One site, two cations, three environments: s^2 and s^0 electronic configurations generate Pb-free relaxor behaviour in a perovskite oxide

T. Wesley Surta†, Thomas A. Whittle†, Matthew A. Wright†, Hongjun Niu†, Jacinthe Gamon†, Quinn D. Gibson†, Luke M. Daniels†, William J. Thomas†, Marco Zanella†, Philippa M. Shepley‡, Yang Li§, Anton Goetzee-Barral§, Andrew J. Bell§, Jonathan Alaria⊥, John B. Claridge†, Matthew J. Rosseinsky†*

† Department of Chemistry, University of Liverpool, Liverpool L69 7ZD, UK

‡ School of Physics and Astronomy, University of Leeds, Leeds LS2 9JT, UK

§ School of Chemical and Process Engineering, University of Leeds, Leeds LS2 9JT, UK

⊥ Department of Physics, University of Liverpool, Liverpool L69 7ZE, UK

ABSTRACT: The piezoelectric devices widespread in society use noncentrosymmetric Pb-based oxides because of their outstanding functional properties. The highest figures of merit reported are for perovskites based on the parent $Pb(Mg_{1/3}Nb_{2/3})O_3$ (PMN), which is a relaxor: a centrosymmetric material with local symmetry-breaking that enables functional properties, which resemble those of a noncentrosymmetric material. We present the Pb-free relaxor $(K_{1/2}Bi_{1/2})(Mg_{1/3}Nb_{2/3})O_3$ (KBMN) where the thermal and (di)electric behaviour emerges from the discrete structural roles of the s^0 K^+ and s^2 Bi^{3+} cations occupying the same A-site in the perovskite structure, revealed by diffraction methods. This opens a distinctive route to Pb-free piezoelectrics based on relaxor parents, which we demonstrate in solid solution of KBMN with Pb-free ferroelectric $(K_{1/2}Bi_{1/2})TiO_3$, where structure and function evolve together revealing a morphotropic phase boundary, as seen in PMN-derived systems. The detailed multiple length-scale understanding of the functional behaviour of KBMN suggests that precise chemical manipulation of the more diverse local displacements in the Pb-free relaxor will enhance performance.

INTRODUCTION

Piezoelectrics are important components of many types of every day technology, employed in applications as varied as radio frequency sensors in cellular phones to ultrasonic transducers for medical imaging.[1] The highest performing materials families locate Pb^{2+} on the A-site of the ABO_3 perovskite oxide structure, which can accommodate a range of local displacements driven by the stereochemically active $6s^2$ electronic configuration of the cation (Figure 1a).[2]

Two stand-out material families have been fundamental for the design of these advanced electro-ceramic components. Solid solution between antiferroelectric $PbZrO_3$ and ferroelectric $PbTiO_3$ affords the $PbTi_{1-x}Zr_xO_3$ (PZT) family, while solid solution between the canonical relaxor (CR) $Pb(Mg_{1/3}Nb_{2/3})O_3$ and ferroelectric $PbTiO_3$ affords the $(1-y)Pb(Mg_{1/3}Nb_{2/3})O_3$-$yPbTiO_3$ (PMN-PT) family. A common feature in these families is the observation of enhanced piezoresponse (d_{33}; 200-600 pm V^{-1} in PZT ceramics; for PMN-PT a d_{33} of 720 pm V^{-1} in ceramics and 2100 pm V^{-1} in single crystals) in a narrow compositional range known as a morphotropic phase boundary (MPB).[3–7] An MPB arises between two ferroelectric phases of distinct symmetry and polarization direction. In PZT, increasing substitution of Ti^{4+} for Zr^{4+} results in a rhombohedral $R3m$ phase with [111] polarization along the body diagonal of the cubic perovskite unit cell transforming to a tetragonal $P4mm$ phase with [001] polarization along the cell edge (Figure 1a), due to ordered displacements of the $6s^2$ Pb^{2+} cation in these directions.[1,3] The complex interplay of chemical bonding and physical response at the MPB continues to be debated in mechanistic terms, but the ability to reorient the electrical polarization between distinct crystallographic directions at low energy cost is felt to underpin the functional performance.[2,6,8–10]

PMN-PT also displays an MPB (Figure 1a), but, in contrast to PZT, it arises from solid solution between ferroelectric $PbTiO_3$ and the canonical relaxor $Pb(Mg_{1/3}Nb_{2/3})O_3$ (PMN, $Pm\bar{3}m$), adding additional complexity.[2,5,11–13] In PMN, the relaxor behavior is driven by disordered displacements of the $6s^2$ Pb^{2+} cation from the A-site centre that create local dipoles. Relaxors are a class of compositionally disordered, centrosymmetric materials that show temperature dependent relaxations in their dielectric response.[13–15] These dipole relaxations are attributed to different sized polar nanoregions (PNRs), arising from chemical inhomogeneity. The interplay of local chemical and dipole ordering responsible for PNRs is currently a topic of intense debate.[16–23] Relaxor properties can express themselves in slightly different ways, but relaxors have been traditionally defined according to the behaviour of PMN, making it the canonical relaxor (CR).[13,14]

The outstanding functional performance of the Pb-based materials discussed above makes their replacement with

Pb-free alternatives, which would be environmentally desirable, challenging. Design strategies for Pb-free systems have focussed entirely on structural and functional analogy with the PZT family by solid solution between Pb-free ferroelectric (FE) parent materials with distinct polarization directions *e.g.,* rhombohedral *R*3*c* ([111]) symmetry in $(Na_{1/2}Bi_{1/2})TiO_3$ with tetragonal *P*4*mm* symmetry in $BaTiO_3$ or $(K_{1/2}Bi_{1/2})TiO_3$ (KBT).[3,24,25].

To pursue the PMN-PT design route to Pb-free piezoelectrics, a Pb-free CR analogue of PMN is needed. We present the Pb-free canonical relaxor $(K_{1/2}Bi_{1/2})(Mg_{1/3}Nb_{2/3})O_3$ (KBMN), produced by substitution of Pb^{2+} in PMN with $(K_{1/2}Bi_{1/2})^{2+}$ on the A-site of the perovskite. This substitution preserves charge balance, maintains the presence of stereochemically active $6s^2$ cations, and has an appropriate mean ionic radius ($(K_{1/2}Bi_{1/2})^{2+}$ = 1.50 Å, Pb^{2+} = 1.49 Å). Previously reported as a rhombohedral ferroelectric,[26,27] our dielectric, polarization, strain, and heat capacity measurements combined with maximum entropy and Rietveld analysis of neutron powder diffraction (NPD) and synchrotron X-ray diffraction data (SXRD), reveal that KBMN is a cubic relaxor, but with key differences from PMN that are attributable to the underlying chemistry. Both materials show local A-site displacements that do not break their centrosymmetric average structures and thus drive their relaxor characteristics, but those displacements differ because of the distinct behaviours of the s^2 and s^0 cations occupying the A-site in KBMN, which generate three distinct local sites in its cubic average structure. These chemical differences result in KBMN having a lower dielectric permittivity, a greater dielectric relaxation, and more entropic degrees of freedom than PMN. We then explore the PMN-PT design route by combining the Pb-free CR KBMN with the Pb-free FE KBT in (1-*x*)KBMN-*x*KBT. The transition through two monoclinic symmetries observed in the SXRD data of this solid solution is exactly that seen in PMN-PT, and affords polarization, strain, and relaxation responses demonstrating that the Pb-free CR-FE system also displays an MPB. This relaxor-ferroelectric (CR-FE) solid solution strategy opens new directions for the design of Pb-free ferroelectrics.

EXPERIMENTAL

Materials were synthesized using standard solid state synthesis methods via a mixed oxide route to prevent formation of pyrochlore impurities. The mixed oxide method has been routinely employed in the synthesis of PMN and PMN-PT for this reason.[28] A columbite precursor ($MgNb_2O_6$) was made by mixing $(MgCO_3)_4Mg(OH)_2{*}5H_2O$ (99.99%, Sigma) and Nb_2O_5 (99.9%, Alfa Aesar) in stoichiometric amounts and ground in an agate pestle and mortar before reacting in an Al_2O_3 crucible at 1450°C for 3 h with a 5°C/min ramp rate on both heating and cooling. Pure $MgNb_2O_6$ was then ground and mixed with stoichiometric amounts of Bi_2O_3 (99.999%, Alfa Aesar), K_2CO_3 (99.99%, Sigma), and TiO_2 (99.999%, Alfa Aesar) in a pestle and mortar to achieve the desired composition. Mixed reagents were then milled in a planetary ball mill (Fritsch, Pulverisette) in zirconia pots with seven 10 mm zirconia balls and 10 mL of ethanol for 15 min, with 10 min pauses, before reversing the milling direction, over 20 cycles. Milled samples were dried at 80°C before being calcined in Al_2O_3 crucible for 3 h with a 5°C/min ramp rate on both heating and cooling. Calcined powders were pressed into 10 mm cylindrical discs, placed in Al_2O_3 crucibles, buried in sacrificial powder of the same composition, covered, annealed twice for 12 h each, with a 5°C/min ramp rate on both heating and cooling, and intermittent grinding to achieve pure phase powders. The calcining and annealing temperature increased with increasing *x* substitution and temperatures can be seen in Table S.1. The composition of these materials was confirmed to be stoichiometric using optical emission spectroscopy with an inductively coupled plasma atomizer (ICP-OES) and by energy dispersive X-ray spectroscopy (EDX). Scanning Electron Microscopy (SEM) and (EDX) were performed with a Hitachi S4800 equipped with an EDX detector from Oxford instruments. Powder samples were dispersed on a carbon tape attached to an alumina stub and coated with a thin film of carbon before performing imaging and EDX. Chemical quantification was performed using Aztec software. EDX correction factors, for the different elements, were estimated measuring the EDX spectra of appropriate standards. Standards purity was confirmed using X-ray diffraction.

The purity of samples was determined in the lab by powder X-ray diffraction (XRD) using a Panalytical X'pert Pro with Co $K\alpha_1$ (λ = 1.788960 Å) radiation. Synchrotron XRD (SXRD) data were collected at the Advanced Photon Source at Argonne National Lab on beamline 11BM (λ = 0.4128370 Å). Samples were prepared by coating a 0.8 mm Kapton capillary and nesting it inside a 1.5 mm Kapton capillary. For neutron powder diffraction (NPD), 8.4562 g of sample was loaded into a 10 mm diameter, thin walled vanadium can. Data were collected on the Polaris diffractometer at ISIS, the U.K. time of flight neutron source, for 120 min. Neutron absorption was corrected by processing NPD data using the experimental composition, mass, and sample volume to ensure peak intensities were representative of the material. Three detector banks were used for analysis with 2θ = 52.21°, 92.59°, and 146.72°, Bank 3, 4, and 5 respectively. Selected Area Electron Diffraction (SAED) on different zone axes was performed on a JEOL 2100+ using a double tilt holder. Powder samples were dispersed on a carbon coated copper TEM grid. ED patterns were simulated using Single Crystal software. All previously mentioned XRD, NPD, and SAED experiments were performed at room temperature. Low temperature XRD data were measured on a Rigaku SmartLab diffractometer using a Mo Kα rotating anode source and a PheniX cooling chamber (Oxford Cryosystems).

All data were analysed using Pawley or Rietveld analysis as implemented in the Topas Academic software package.[29] X-ray peak profiles were fit with the Stephens model[30] to account for micro strain and a Gaussian size contribution and NPD profiles were fit with a pseudo-Voigt function. Backgrounds were fit with a Chebyshev polynomial function with twelve terms for X-ray data and eighteen terms for NPD data. For Rietveld refinements of KBMN, initial Pawley configurations were used as initial models, with fixed backgrounds, instrumental parameters and profile parameters. Atomic positions and isotropic displacement parameters were constrained to be equal for different cations on a shared site. Anisotropic displacement parameters were used on the oxygen position. Split oxygens sites and anisotropic displacement parameters and were both

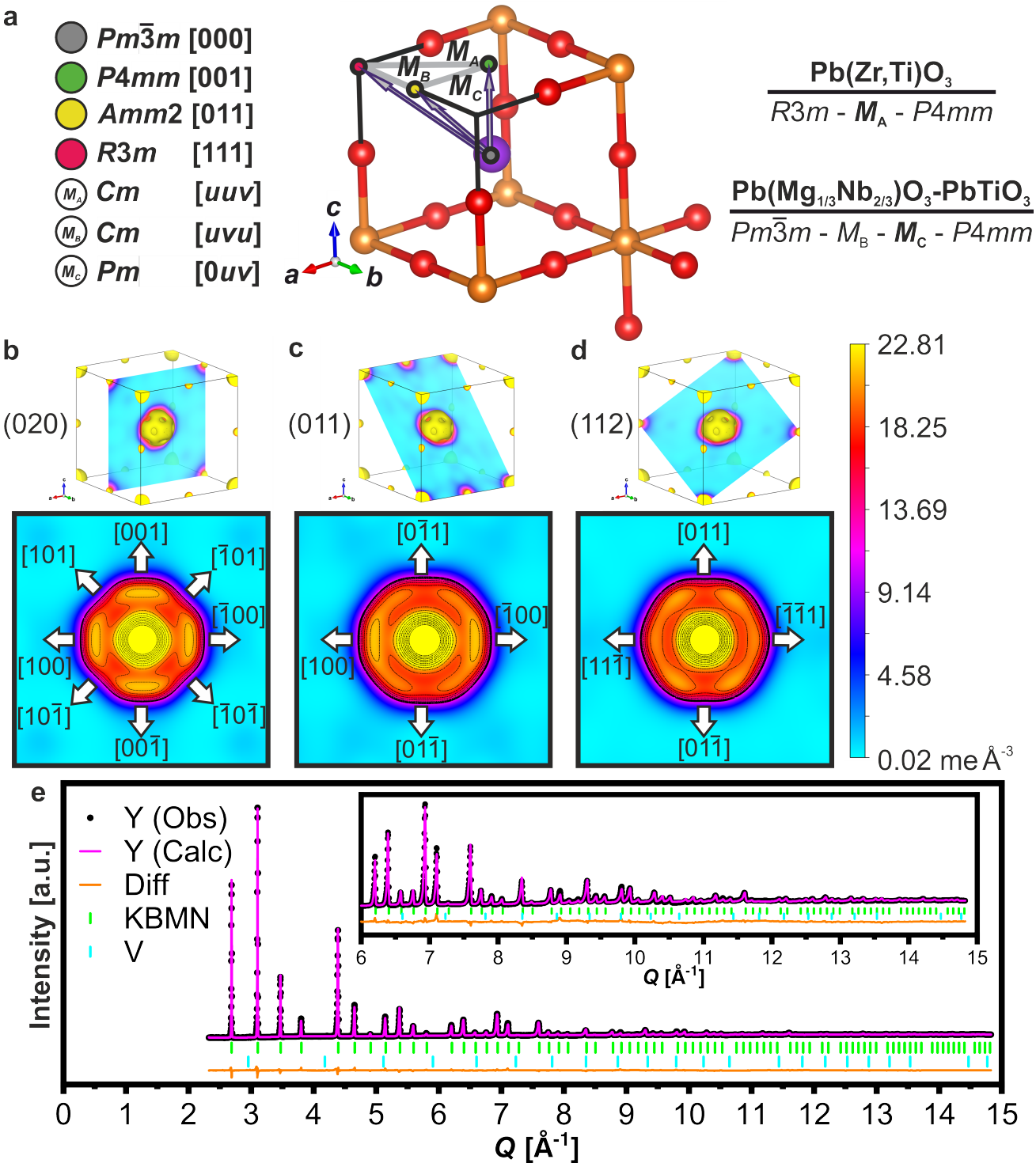

Figure 1. a) Diagram illustrating the $Pm\bar{3}m$ cubic aristotype for ABO_3 perovskite, and displacements of the A-site that create polarization. The A-site, B-site, and oxygens are shown in purple, orange, and red respectively. Displacement directions are shown and the resulting symmetries are listed. Displacement directions, in brackets, are all relative to the cubic cell, whereas lattice planes, in parentheses, are relative to the cubic cell only if the subscript c is used. Displacements lying on mirror planes result in monoclinic symmetry, which are illustrated as grey lines in the top left. For example *Cm* symmetry represents polarization in the $(011)_c$ mirror plane. Proposed phase progressions for PZT and PMN-PT are listed, with the MPB symmetry in bold. b-d) Calculated electron density distribution from maximum entropy method analysis of SXRD data and the contour plots of A-site cross sections corresponding to the b) (020), c) (011), and d) (112) planes. Arrows have been added to the cross sections to illustrate displacement directions associated with [001], [011], and [111] displacements. Results of combined Rietveld refinement of SXRD and three sets of NPD data, with the e) high resolution NPD data (Bank 5, Polaris) shown, using the disordered cubic model with three A-sites, K^+ in the centre, and Bi^{3+} displaced along [001] and [111], and anisotropic displacement parameters on the oxygen. Observed data are black circles, calculated is a magenta line, the difference is an orange line, *hkl* ticks for KBMN are green, and *hkl* ticks for the vanadium sample holder are cyan. The high *Q* region is inset.

investigated, but the latter model yielded better fits reducing the R_{wp} from 4.85% to 4.33% and improving the visual fit. Occupancies of all sites were restrained to match the target stoichiometry as these were confirmed using analytical methods. Refinement of the occupancies were attempted, but resulted in occupancies greater than one, leading us to constrain the occupancies to the measured stoichiometry. Additional A-site positions in the [001] and [111] directions were added by analysing maximum entropy method (MEM) outputs and determining displacement magnitudes. The atomic positions of K^+ and Bi^{3+} were constrained to be the same when on the same displaced site to ensure that the displacement magnitudes were equal. Occupancies on A-sites were restrained to match the stoichiometry, factoring in the site occupancy. The occupancy of the K^+ and Bi^{3+} were initially constrained to be equal across the three A-sites in the model ([000], [001], and [111]). Attempts to refine of a [011] displaced site always resulted in a zero occupancy. All atomic positions, atomic displacement parameters, lattice parameters, profile parameters, backgrounds, zero errors, and occupancies were refined to yield the final structural model. A crystallographic information format (CIF) file has been submitted with this publication. Root mean square displacements of bonds were calculated by accounting for how Bi^{3+} and O^{2-} atomic displacements, and their errors, impact the distribution of possible bond lengths for each displaced A-site. The atomic displacement contribution from O-sites was determined by finding the displacement along the trace of the anisotropic strain tensor where the bond vector intersects it. All MEM inputs were created using Jana2006,[31] 3D electron density distributions were calculated with BayMEM,[32] and outputs were visualized in VESTA.[33]

Pure phase powders were sintered into dense ceramics using spark plasma sintering (SPS) in a Thermal Technology LLC DCS10 furnace. Samples (~ 0.75 g) were loaded into a 10 mm diameter graphite die lined with a graphite foil and loaded into a sample chamber which was evacuated and backfilled with He three times. Sample was pressed uniaxially at 60 MPa and heated to the desired temperature at a rate of 200°C/min, held for 1 min, and cooled at the same rate. The sintering temperatures for each composition can be seen in Table S.1. Temperatures were controlled by a pyrometer through a bore hole in the side of the die, the emissivity of the die set was not accounted for, so the true temperature of the powder during pressing likely varied from the measured value. These discs were then heated in a tube furnace under O_2 atmosphere at the calcining temperature for 12 h with a 5°C/min ramp rate on heating and cooling. Firing disks under O_2 allowed for the oxidation of any residual graphite from the surface of the pellets as well as relieving any residual stress from the interface of grains. This process resulted in pure phase pellets with densities of 95% of the crystallographic density or greater as determined by the Archimedes method.

Dense pellets were polished on a Struers automatic polishing machine using #800 and #1200 SiC foils (Struers). Pellets for dielectric measurements were polished down to a thickness 500-900 +/- 10 μm. High temperature gold paste (Koartan 4129) was used to form electrodes and was painted on faces of the cylinders and fired on at 650°C for 30 min with a 5°C/min ramp rate on heating and cooling. Dielectric permittivity (ε´) and loss tangent (tan(δ)) were measured using an Agilent 4980A and a home built sample holder and a program created in LABVIEW.[34] Data were collected from room temperature to 600°C on heating and cooling and reported on cooling. Curie-Weiss fitting was done on the high temperature linear region of the inverse ε´ and the Burns temperature was determined to be where the 1/ε´ deviated from that Curie-Weiss fit.[35] Low temperature dielectric and thermally stimulated depolarization current (TSDC) measurements were performed in Delta 9023 environmental test chamber under liquid nitrogen.

Samples for piezoelectric and ferroelectric measurements were polished in a similar way to dielectric samples but to a thickness of 150-400 +/- 10 μm and subsequently polished to a mirror finish with #4000 SiC foil (Struers). Gold electrodes were attached to surfaces by sputtering discs for 60 sec on each face. An aixPES (aixACCT GmbH, Germany) was used to perform $P(E)$, $S(E)$ and $I(E)$ measurements at room temperature. The maximum polarization (P_{max}) and the remnant polarization (P_r) were taken from $P(E)$ loops under positive electric field at 80 kV/cm. The coercive field (E_c) was determined as the peak of the current in $I(E)$ data, under positive field at 80 kV/cm. $P(E)$ data on KBMN were measured at 200 K in a Delta 9023 environmental chamber under liquid nitrogen using a Radiant Ferroelectric Test Kit. Electric fields were applied to samples while submerged in silicone oil in order to prevent electrical breakdown and all measurements were done at 1 Hz. Samples for TSDC were heated to 413 K then field cooled at 60 kV/cm to 100 K at a rate of 1 K/min. Once reaching temperature the sample was short-circuited to dissipate any accumulated charge for 30 min before heating, leaving only current from intrinsic polarization. Current was measured with a Keithley 6430 subfemtoamp remote source meter while heating at 1 K/min. Polarization was calculated by integrating the current with respect to time using the equation:

$$P = \int_{t1}^{t2} \frac{i}{A} dt$$

where P is the polarization, t is the time, A is the area of the sample, and i is the current.

Heat capacity measurements were performed on dense pellets that have been made into rectangular shapes to fit in the instrument. Data from 1.8–350 K were measured on a Quantum Design Physical Properties Measurement System (PPMS) using the heat capacity option. The heat capacity values were determined by the relaxation method. The sample was affixed to the stage using N-grease from 1.8-250 K and using H-grease from 250-350 K, the contribution of which to the heat capacity was subtracted by measuring an addenda prior to sample measurement. Three data points were collected at every temperature to measure an average. Data from 313 – 967 K were collected on a Netzsch Pegasus 404 DSC with a Pt furnace attachment in a Pt crucible under a 50 mL/min flow of N_2. Heat capacity was determined from heat flow by the ratio method comparing to a sapphire crystal measured in exactly the same way. The heat capacity data were analysed in Mathcad using a linear combination of Debye functions with the general formula:

$$\frac{C_p}{Nk} = 9\left(\frac{\mathrm{T}}{\Theta_D}\right)^3 \int_0^{\Theta_D/\mathrm{T}} \frac{\left(\frac{h\nu}{k\mathrm{T}}\right)^4 e^{\frac{h\nu}{k\mathrm{T}}}}{(e^x-1)^2} d\frac{h\nu}{k\mathrm{T}}$$

where Θ_D is the Debye temperature, T is temperature, N is the number of atoms in the solid, k is the Boltzmann constant, h is Planck's constant and ν is the Debye frequency. The Einstein functions used had the general formula:

$$C_p = 3Nk\left(\frac{\Theta_E}{2\mathrm{T}}\right)^2 \frac{1}{\sinh^2\left(\frac{\Theta_E}{2\mathrm{T}}\right)}$$

where Θ_E is the Einstein temperature, T is temperature, N is the number of atoms in the solid, and k is the Boltzmann constant. The Einstein contribution represents that of localized oscillators with a singular vibrational frequency, and thus represents non-propagating modes, in contrast to the propagating phonons of the Debye model.

A linear term (γ) was also found to be necessary to fit the heat capacity. Usually, these terms are attributed to the electronic contribution to the heat capacity, but it can also be from any two level quantum system wherein an atom can tunnel between two states, and is found to be present in disordered solids.[36,37] This term is likely to then be due to the disorder present in the material which can create atomic positions that are close in energy. The contributions from the two Θ_D, three Θ_E, and the γ were found to be 0.35 for Θ_{D1} (280 K), 0.6051 for Θ_{D2} (803 K), 0.0006 for Θ_{E1} (27 K), 0.0069 for Θ_{E2} (50 K), 0.0374 for Θ_{E3} (81 K), and 0.45 for γ (3.182×10^{-5} J mol^{-1}K^{-2}).

To calculate the additional C_p from dipoles, the calculated C_p from our phenomenological model was subtracted from the measured C_p by interpolating the value of the measured C_p for each calculated value. The additional C_p was then divided by the temperature and integrated over the temperature range to determine the dipole entropy, divided by the gas constant (R) to normalize the value, and multiplied by the atoms per formula unit to determine the entropy per atom. To calculate the dipole entropy per Bi^{3+}, this value was multiplied by two.

RESULTS AND DISCUSSION

Synthesis of (1-x)KBMN-xKBT required the mixed oxide method using a $MgNb_2O_6$ precursor to suppress pyrochlore impurities, adapted from PMN-PT.[28] Full synthetic and ceramic processing details can be found in the Supplementary Information (Table S1, Figure S1). Materials were confirmed to be stoichiometric by SEM-EDX and ICP-OES (Figure S2a-b). KBMN was first compared to PMN structurally, at room temperature. SXRD patterns index to $Pm\bar{3}m$ symmetry and Pawley fits show no signs of symmetry lowering (Tables S2-3). Rietveld refinement of these data in $Pm\bar{3}m$ symmetry yield a high quality fit, (Figure S3, Tables S4-5), but A-site isotropic displacement parameter (B_{iso}) are 10.90(18) Å^2. Relatively high A-site B_{iso} of 3 - 4.5 Å^2 are common in CRs such as PMN, $Pb(Sc_{1/2}Nb_{1/2})O_3$, and $(K_{1/2}Bi_{1/2})(Sc_{1/2}Nb_{1/2})O_3$.[38–41] Fourier difference analysis of SXRD fits (Figure S4) reveals missing electron density from the model, distributed isotropically around the A-site. Fourier difference analysis of NPD data (Figure S5) shows oxygen disorder, which was better modelled with anisotropic displacement parameters than multiple oxygen sites, as described above in the experimental section.

To investigate the local structural origin of the large A-site B_{iso}, we analysed SXRD data using the maximum entropy method (MEM), which reconstructs the electron density directly from the measured Bragg intensities.[31,32] The resulting 3D electron density distributions can be seen in Figures 1b-d and accurately reproduce the perovskite structure, but the A-site distribution is clearly and distinctly non-spherical. Contour plots of (020), (011), and (112) lattice planes can be seen in Figures 1b, c, and d respectively. The electron density shows a maximum for the central A-site position (1/2, 1/2, 1/2) - another maximum is displaced along the <001> directions. There is a continuous distribution of electron density from <001> to <111> directions, which is reduced in the <011> directions.

Guided by the MEM analysis, we created a structural model for Rietveld refinement with three A-sites in order to capture the measured electron density; one central site ([000]) and two additional sites corresponding to displacements along [001] and [111]. Displacements in [011] directions were attempted, but were found to not contribute, as described above in the experimental section. The atomic positions, B_{iso}, and occupancies for K^+ and Bi^{3+} on each A-site were constrained to be equal, but these parameters were allowed to refine independently for each A-site as the high Q diffraction data permitted this. The atomic displacement parameters, displacement magnitudes of [001] and [111] A-sites from the A-site centre, and A-sites occupancies were refined simultaneously while restraining the overall composition to match the measured stoichiometry. The resulting combined refinement has reasonable B_{iso} values (Table S6) and fits the NPD data well (Figure S6), but has large intensity mismatches with SXRD data. Refinements against SXRD data only result in different occupancies and large intensity mismatch with NPD data. The observation of two local minima separately consistent with X-ray and neutron data led us to allow different K^+ and Bi^{3+} occupancies on each of the three A-sites to account for the scattering contrast, while continuing to restrain the overall composition to maintain the measured stoichiometry. This allowed the model to rapidly converge to fit both data sets very well simultaneously (Figure S7) and afforded reasonable structural parameters (A-site $B_{iso} \leq 1.6$ Å^2, Table S7). The separation of the K^+ and Bi^{3+} occupancies on the three components of the A-site led, within error, to solely K^+ occupancy of the [000] position at the A-site centre, with only Bi^{3+} on the displaced, lower point symmetry [001] and [111] sites. This led us to restrict the K^+ to the [000] site and let Bi^{3+} refine on the other sites (Figure 1e and S8). All bond lengths and bond valence sums (Table S8) in this final model are reasonable.

Table 1. Refined parameters resulting from Rietveld analysis of $(K_{1/2}Bi_{1/2})(Mg_{1/3}Nb_{2/3})O_3$. The lattice parameter, agreement indices, atom type, the site (as it is referred to in text), Wyckoff positions, the point group of the site, atomic positions, occupancies, percentage of the A-site occupancy calculated from refined occupancies, the isotropic displacement parameters, and the anisotropic displacement parameters are all listed. The isotropic trace of the anisotropic displacement parameters (B_{eq}) is listed in brackets under B_{iso}. All values with errors have been refined simultaneously. The A-O bond lengths for the three different A-sites are listed at the bottom, all bond lengths are summarized in Table S8.

Pm$\bar{3}$m	a = 4.046490(4) Å		R_{wp} = 4.06 %		R_p = 1.45 %		G.O.F = 2.79				
Atom	**Site**	**Wyckoff Position**	**Point Group**	***x***	***y***	***z***	**Occ**	**A-site %**	**B_{iso} (Å^2)**	**B_{11} (Å^2)**	**B_{22} / B_{33} (Å^2)**
K^+	[000]	1b	*m*$\bar{3}$*m*	0,5	0,5	0,5	0,5	50	1.02(3)		
Bi^{3+}	[001]	6f	4*mm*	0,5	0,5	0.6484(17)	0.053(2)	32(2)	1.64(10)		
Bi^{3+}	[111]	8g	3*m*	0.5842(11)	0.5842(11)	0.5842(11)	0.0231(18)	18(2)	0.40(11)		
Mg^{2+}	B-site	1a	*m*$\bar{3}$*m*	0	0	0	1/3		0.871(6)		
Nb^{5+}	B-site	1a	*m*$\bar{3}$*m*	0	0	0	2/3		0.871(6)		
O^{2-}	O-site	3d	4/*mmm*	0	0	0,5	1		[1.708(6)]	2.869(6)	1.126(6)
A-O Bond Lengths											
K [000] - 2.861301(2) Å × 12											
Bi [001] - 2.473(4) Å × 4, 2.9236(14) Å × 4, 3.313(6) Å × 4											
Bi [111] - 2.404(4) Å × 3, 2.9215(16) Å × 6, 3.360(5) Å × 3											

The refined parameters are shown in Table 1 and the refined structure is shown in Figure 2a. The s^0 K^+ cations occupy the cubic symmetry [000] position (*m*$\bar{3}$*m* point group, Figure 2b) and the s^2 Bi^{3+} cations are displaced away from it. Of the total A-site cations, 32(2)% are Bi^{3+} on the *4mm* symmetry [001]-displaced position (Figure 2c) and 18(2)% are Bi^{3+} on the *3m* symmetry [111] position (Figure 2d). B-site polyhedra are shown in Figure S9. The local displacements of Bi^{3+} from the A-site center correspond to local dipoles, and their inability to drive global symmetry lowering provides a route to the possible formation of polar nanoregions (PNRs) through shorter-range correlation. Previously reported disordered cubic perovskites have refined a single A-site that is displaced from the site centre and thus not distinguished the roles of s^0 and s^2 configurations.[38–44] We are able to distinguish the average structure effect of these different chemistries in creating three sites, which are differentially occupied in a manner that is driven by the contrast in electron configuration between K^+ and Bi^{3+}. This is because of the *Q* range, counting statistics and scattering contrast of the two datasets. The A-site displacements in KBMN are 0.6005(17) Å along [001] and 0.5901(11) Å along [111], whereas PMN and $(K_{1/2}Bi_{1/2})(Sc_{1/2}Nb_{1/2})O_3$ have displacements of 0.31 Å along [111] and 0.44 Å along [001] respectively.[39,41] The displacements in KBMN are therefore the largest seen in a disordered cubic model, but result in more reasonable bonding environments for Bi^{3+}.

Figure 2e shows the A-O bond lengths and root mean squared (rms) displacement for both K-O bonds and the shortest of the Bi-O bonds in [001] and [111] polyhedra. The shortest Bi-O bonds are in the direction in which the A-site is displaced (Table S9-10). The rms displacement accounts for how the bond vector intersects the oxygen anisotropic displacement tensor. For the two BiO_{12} polyhedra in KBMN the Bi-O bond lengths are very close to those observed for the 100% Bi^{3+} A-site perovskites $Bi(Zn_{1/2}Ti_{1/2})O_3$ (BZT, [001] ordered A-site displacement *P*4*mm*, shortest Bi-O 4 × 2.384 Å) and $BiFeO_3$ (BFO, [111] ordered A-site displacement *R*3*c*, shortest Bi-O 3 × 2.365 Å) that feature the same displacement directions, as seen in Table S8.[45,46] Lower valence A-sites (K^+, Pb^{2+}) have longer bond lengths than Bi^{3+}. The bond lengths for both PMN (2.861 Å, [000], *Pm*$\bar{3}$*m*) and $KNbO_3$ (2.763 Å, [011], *Amm*2) are longer than the measured Bi-O bond lengths in KBMN, and are at the maximum of the rms displacement (2.772 Å) for the [001] displaced Bi^{3+} in KBMN.[47,48] For disordered cubic models of PMN with [111] displacements, the Pb-O bond length (2.599 Å) is closer to Bi-O bonding environments, but still at least 0.126 Å longer. The A-site bond lengths in PMN ([000]) and $KNbO_3$ are comparable to the isotropic KO_{12} bond length (2.861301(2) Å) in KBMN. The local symmetries of all cations are labelled in Table 1. The Rietveld model can only define one oxygen position, so additional information about local displacements is contained in the atomic displacement parameters. The bonding environments observed highlight the different structural roles of these ions. The smaller, $6s^2$ Bi^{3+} undergoes substantial (≈ 0.6 Å) displacements from the A-site centre in two distinct directions to satisfy valence requirements, breaking symmetry locally consistent with the bonding expected from its electronic configuration and creating a dipole at each A-site occupied by Bi^{3+}, while the larger, spherical K^+ maintains its centrosymmetric position thus preventing octahedral rotation driven by Bi^{3+}. Direct analysis of the electron density through MEM represents a new approach for studying relaxors. MEM analysis would be interesting to apply to other relaxors, such as PMN, and raises questions of whether these disordered cubic systems have [000] sites. In cubic perovskite oxides, chemical preference for local scale A-site displacements has only ever been seen in $0.6BaTiO_3$-$0.4BiScO_3$ (300 K, *Pm*$\bar{3}$*m*) and KBT (673 K, *Pm*$\bar{3}$*m*) using reverse Monte Carlo modelling of total scattering data.[49–51] The observation of disordered cubic average structure with local cation displacements creating dipoles is consistent with a CR – the *Q* resolution of the data allow high confidence in the diagnosis of cubic symmetry for KBMN.

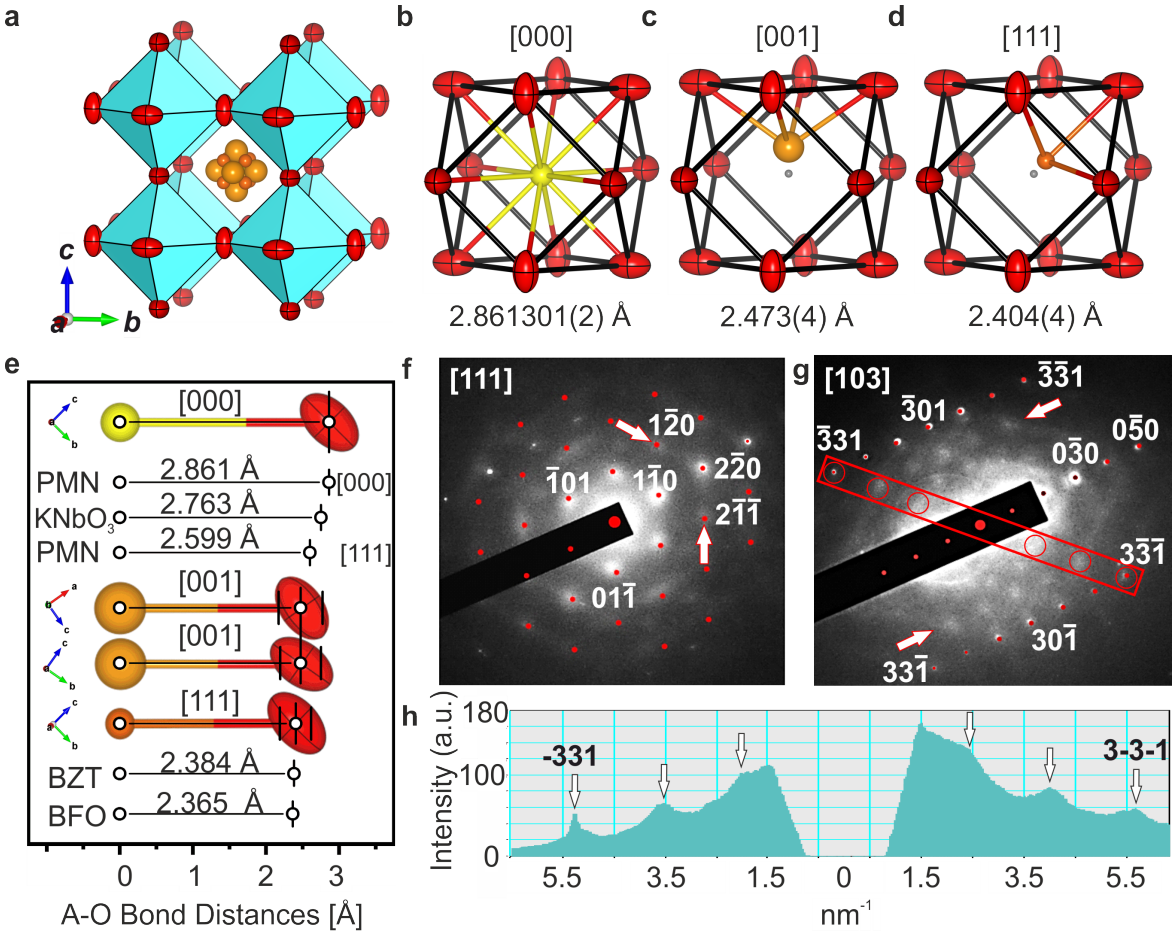

Figure 2. a) Final refined structure from Rietveld analysis of $(K_{1/2}Bi_{1/2})(Mg_{1/3}Nb_{2/3})O_3$. The [000] A-site is yellow, [001] sites are orange, [111] sites are red-orange, B-sites are shown as cyan octahedra, and oxygens are shown as red displacement ellipsoids (90% probability). The size of all atoms are representative of the refined atomic displacement parameters. The polyhedral environments of the b) [000], c) [001], and d) [111] A-sites are shown. The polyhedral centroid is shown as a light grey sphere and shortest A-O distances within the respective polyhedra are both shown as bonds and the value is listed. e) Bond lengths for the [001] and [111] A-sites, where the error bars account for the rms displacements of both the A-site and the O atoms. The rms displacement of the oxygen atom is calculated from its anisotropic displacement tensor in the direction of the A-O bond vector. Average bond lengths are shown as white circles, and the [000] A-site, PMN, $KNbO_3$, [001] A-site (intersecting the O two different ways), the [111] A-site, $Bi(Zn_{1/2}Ti_{1/2})O_3$ (BZT), and $BiFeO_3$ (BFO) are shown to illustrate that the displaced A-sites are more consistent with Bi^{3+} environments. Selected area electron diffraction data (SAED) along f) [111] and g) [103] zone axes is shown in black and white, with calculated *hkl* Bragg reflection positions displayed in red. Selected reflections have been indexed for clarity. Arrows have been added to the [111] zone axis to call attention to sheets of diffuse scattering between the $2\bar{2}0$ Bragg reflection and both $1\bar{2}0$ and $2\bar{1}\bar{1}$ Bragg reflections. A red box has been added to the [103] zone axis which lies in the $[\bar{3}31]$ direction, the line profile of which is shown in h). Arrows in the line profile highlight sheets of diffuse scattering that are indicated by the red circles in the [103] zone axis.

The Rietveld and MEM analyses determine the average structure and capture local disorder. Intermediate length-scale pair correlations are revealed in selected area electron diffraction (SAED) data (Figures 2f-g). Diffuse scattering is observed between Bragg reflections along the [111] zone axis (Figure 2f) and as lines across the [103] zone axis (Figure 2g), which indicates correlations between dipoles. The same sheets of diffuse scattering seen in the [111] zone axis are present in PMN[52] and give rise to linear diffuse streaks running along adjacent zone axes. In the [111] zone axis, sheets about the $(2\bar{2}0)$ reflection project towards adjacent $(1\bar{2}0)$ and $(2\bar{1}\bar{1})$ reflections, which have been marked with arrows in Figure 2f.[52] These transverse {111}* sheets of diffuse scattering originate from linear correlations of cation displacements. The sheets of diffuse intensity are clearly observable in the line profile (Figure 2h) across the [103] zone axis. Along the [103] zone axis, in addition to diffuse sheets there are diffuse superlattice reflections observable, marked by arrows in Figure 2g. Diffuse superlattice reflections of this nature are indicative of nanoscale cation ordering. In PMN, diffuse superlattice reflections have been observed in SAED[52–54], and single crystals[16,21,55,56], which arise from rock-salt type ordering of the B-site cations. KBMN has the same B-site sublattice as PMN. These nanometer-scale chemically-ordered regions with 1:1 ordered Mg^{2+} and Nb^{5+} cations, within a Nb^{5+} rich matrix, aid in the formation of PNRs in PMN.[16,56] This observation of diffuse scattering in KBMN suggests that the local dipoles observed in the average structure refinement are correlated. The nature of these correlations, the roles of the A-site and B-site sublattices in these diffuse features, and the correlation lengths are all important parameters to understand to further in order to

deepen the analogy to, and differentiate from, PMN. Quantitative analysis of the diffuse scattering would likely require single crystal diffuse scattering data, as the data acquisition times for SAED were limited due to sample damage from the electron beam. The diffuse scattering illustrates both that cation displacements are correlated and that B-site cations order on intermediate length scales. The local cation displacements identified in the average structure and these intermediate range correlations together are consistent with the formation of PNRs, in analogy with PMN.

The signature of relaxor properties is in the dielectric response. The temperature dependence of the real (ε′) and imaginary (ε′′) dielectric permittivity (Figure S10) from 300 to 900 K shows a peak (T_m) in ε′ at 413 K in 1 MHz data. Curie Weiss fitting of 1 MHz data yields a Weiss constant (θ_W) of -2675 K; indicating antiferroelectric correlations, consistent with SAED. At low frequency T_m is not clearly visible, particularly in ε′′ data, indicating that the measurement ends in the middle of a frequency-dependent phase transition. To observe the full phase transition, ε′ and ε′′ were measured from 100 to 500 K (Figure 3a) to identify T_m for all frequencies. The frequency dependence of T_m from 1 MHz to 1 kHz (ΔT_m) is determined to be 98 K. In PMN T_m is 266 K at 1 MHz, ΔT_m is 18 K, and the ε′ at T_m (ε'_{max}) is 12,000.[57] The dielectric response of KBMN is in contrast to this, notably the ε'_{max} of 220. A decrease in ε'_{max} by two orders-of-magnitude is seen in $(Pb_{1/2}Ba_{1/2})(Mg_{1/3}Nb_{2/3})O_3$, indicating the decrease in ε′ is associated with the removal of half of the s^2 cations.[58] This reduction in s^2 cation content is likely not the only mechanism resulting in low permittivity, as the large off-centroid displacement in the absence of electric field or the diversity of possible polarization vectors that within PNRs may also reduce the response, revealing another key nuance differentiating the A-site chemistry of KBMN and PMN.[59] The relaxation mechanisms were investigated using Vogel-Fulcher analysis (Figure 3b), which yields a freezing temperature (T_f = 193 K) and activation energy (E_a = 0.0330 eV) for glass-like dipoles. KBMN has a ΔT_m that is almost 5 times that of PMN. The larger ΔT_m indicates a larger size distribution of PNRs, but their activation energy is similar to PMN (E_a = 0.0786 eV).[60] A larger ΔT_m is consistent with the Rietveld analysis of KBMN, which shows two large local A-site displacements instead of the single smaller displacement seen in PMN. The additional displacement coupled with the large variety of ferroelectric and antiferroelectric correlations possible, leading to more diverse PNRs, then readily explain large dielectric relaxations observed. The shorter A-O bond lengths for Bi^{3+} than Pb^{2+} would lead to stronger interactions between correlated dipoles, explaining the similar activation energies and higher T_m in KBMN.

Our design strategy was to make a Pb-free CR, which requires we preclude dipole glass or relaxor ferroelectric (RFE) mechanisms. A CR has globally centrosymmetric structure which is maintained below dielectric transitions, despite measurable polarization, with no ferroelectric symmetry appearing in average structural data.[13,14] A dipole glass and RFE both have dielectric relaxations, but the

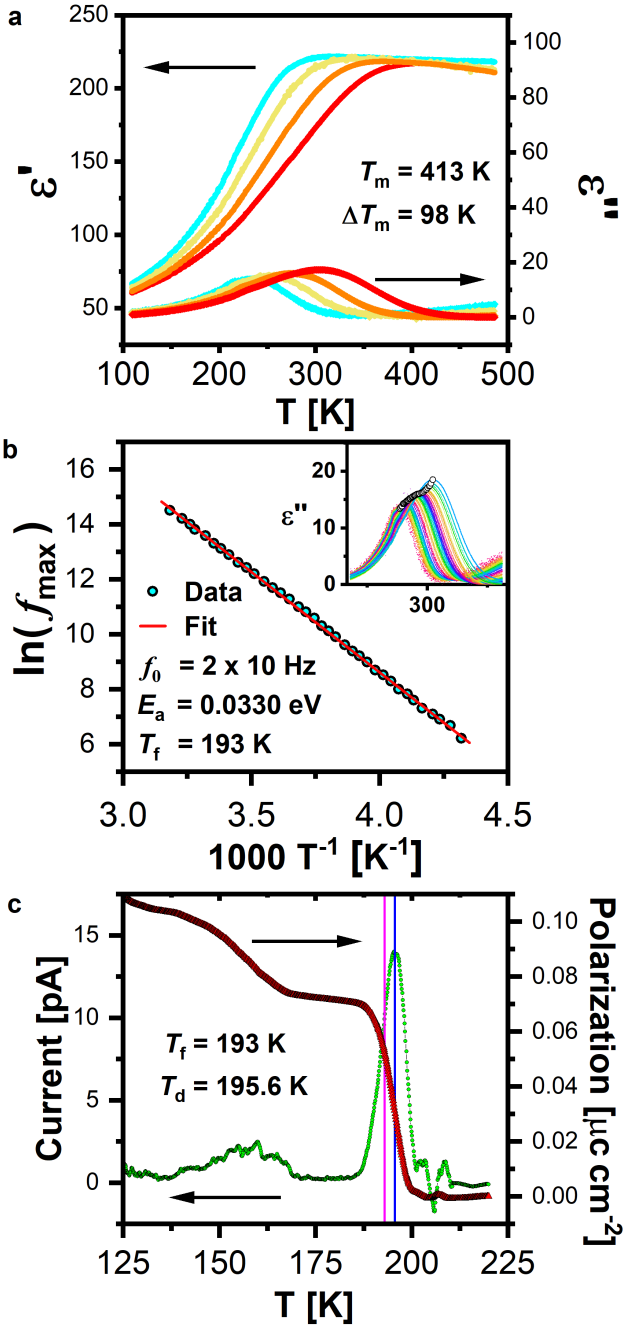

Figure 3. a) Temperature dependence of real (ε′) and imaginary (ε′′) dielectric permittivity of KBMN. 1 kHz (cyan), 10 kHz (yellow), 100 kHz (orange), and 1 MHz (red). The temperature of ε'_{max} (T_m) at 1 MHz and the difference in T_m from 1 MHz to 1 kHz (ΔT_m) are shown. b) The frequency dependence of T_m fit using Vogel-Fulcher analysis. T_m values are cyan circles and the fit a red line. T_m values taken from ε′′ collected from 500 Hz to 2 MHz, labelled with white circles in the inset. The critical frequency (f_0), activation energy (E_a), and freezing temperature (T_f) are shown. Thermally stimulated depolarization current, showing the measured current in green and the polarization (red) derived from the integration of current with respect to time. The depolarization temperature (T_d) determined from this measurement and the freezing temperature (T_f) from Vogel-Fulcher analysis are labelled in blue and magenta respectively.

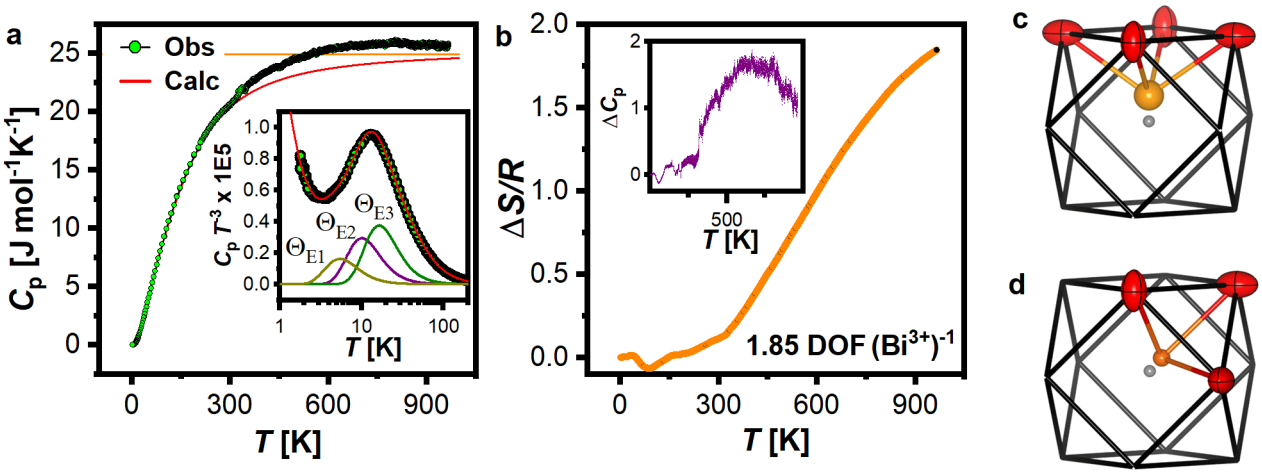

Figure 4. a) Temperature dependence of the heat capacity (C_p) of KBMN shown as green circles and the fit of the phonon contribution is the red line. The orange line is the Dulong-Petit limit, which is three times the gas constant ($3R$) and represents the maximum phonon contribution. The model consists of two Debye functions (Θ_D), three Einstein functions (Θ_E), and a residual linear term (γ). The $C_p T^{-3}$ is inset in c) and illustrates that the model fits well at low temperature and that three Θ_E are necessary, shown as Θ_{E1} in dark yellow, Θ_{E2} in purple, and Θ_{E3} in green. d) The additional degrees of freedom per Bi^{3+} beyond phonons as a function of temperature are shown in orange, which come from the integral of the additional C_p (excess over the phonon fit in c), shown in the inset. Local dipole degrees of freedom associated with the center-of-symmetry-breaking displacements on the A-site in both e) [001] and f) [111] directions.

ground state dipole configuration lead to either no polarization or a ferroelectric symmetry below T_m, respectively. The ground state configuration of dipoles was investigated by measuring $P(E)$ loops at room temperature and 200 K. Room temperature $P(E)$ data (Figure S11a) shows a linear response, consistent with a lossy dielectric (tan(δ) = 0.122). At 200 K (Figure S12) loops are still linear, but the slope of the loops increases with increasing applied field, indicating polarization of domains, but saturation is not observed at fields up to 100 kV cm^{-1}.[61] A high coercive field is consistent with the large Bi^{3+} off centring, another distinction between KBMN and PMN. To further confirm polarization, electrical current was measured while heating poled samples. The thermally stimulated depolarization current (TSDC; Figure 3c) shows a peak for the depolarization temperature (T_d) at 195.6 K, which is close to the calculated T_f (193 K). The feature in the current response below 170 K is an experimental artifact from the freezing dielectric fluid. This low temperature feature was also seen when measuring transition-free standard Al_2O_3, where no feature at 195.6 K is observed. Lastly, variable temperature XRD was measured from 295 – 12 K (Figure S13). These data show no indication of new reflections or peak splitting through the temperature range. Pawley fitting of these data yield a smooth change in lattice parameters (Figure S14) with no sign of changes in symmetry. The observations of polarization in TSDC and $P(E)$ data, the lack of emergent ferroelectric properties in $P(E)$ data, and the maintenance of a globally cubic symmetry well below T_m, T_d, and T_f allow us to classify KBMN as a CR.

The classification of KBMN as a CR through dielectric and polarization data adds insights into our structural analysis. The observation of local Bi^{3+} displacements through MEM and Rietveld analysis, the diffuse sheets representative of correlated cation displacements, and the diffuse superlattice reflections from B-site ordering indicates dipoles, correlation of those dipoles, and local chemical ordering, respectively. These correlations are consistent with the observed relaxor behavior, which arises from the dynamics of regions of correlated polarization vectors (PNRs), which are confirmed via dielectric and polarization data. The details of whether [001] and [111] displacements aggregate with, or separate from, each other and their correlations with rock-salt ordered regions are not available from these data.

Relaxor properties arise from freezing of dipole degrees of freedom, which is thermodynamically quantifiable, as the excess entropy over the phonon contribution to the heat capacity arises from this freezing. Thus the heat capacity (C_p) of KBMN was measured as a function of temperature (Figure 4a). The phonon contributions to C_p were modelled from 1-1000 K with two Debye functions (Θ_{D1} = 280 K, Θ_{D2} = 803 K), three Einstein functions (Θ_{E1} = 27 K, Θ_{E2} = 50 K, Θ_{E3} = 81 K), and an additional linear term ($\gamma = 3.182 \times 10^{-5}$ J mol^{-1}K^{-2}). The KBMN model is more complex than PMN which has one Debye function (Θ_D = 165 K), two Einstein functions (Θ_{E1} = 28 K, Θ_{E2} = 60 K)[37] and a linear contribution, attributed to tunnelling of atoms through non-degenerate states in a two-well potential,[36] which can arise from the distribution of local environments in a relaxor. This enhanced complexity can be associated with the larger chemical heterogeneity arising from the more complex A-site chemistry and local displacement patterns (Table 1, Figure 2a) quantified in the average structure of KBMN.

Above 200 K, the measured C_p diverges from this phonon model. The divergence arises due to additional entropy from melting dipoles, and is at a temperature consistent with the onset of dielectric relaxations (Figure 3a), the calculated T_f (193 K), and T_d (195.6 K) from TSDC (Figure 3c). The additional entropy from dipoles can be quantified, the integral of which (Figure 4b) gives the additional degrees of

freedom (DOF) arising from the dipoles. The integration yields 0.92 DOF A-site^{-1} from dipole entropy, slightly smaller than the 1.1 DOF A-site^{-1} seen in PMN.[62] This result is consistent with the refined average structure, with KBMN having 1.85 DOF $(Bi^{3+})^{-1}$ and two Bi^{3+} displacement directions along [001] and [111] (Figures 4 c-d), compared to PMN having 1.1 DOF $(Pb^{2+})^{-1}$ and one [111] displacement. These C_p data further strengthen the assignment of KBMN as a CR by identifying the excess entropy associated with the two displacement directions that form the local A-site dipoles. The difference in excess entropy between PMN and KBMN also highlights the distinct chemical differences arising from the A-site chemistry. The additional degree of freedom presents an opportunity for additional tuning of functional properties, which is not available in PMN.

To increase the operational temperature of PMN and improve the piezoresponse through formation of an MPB, solid solution with FE PT is needed. Therefore, we explored the formation of an MPB from the Pb-free CR KBMN through solid solution with the Pb-free FE KBT. The solid solution (1-*x*)KBMN-*x*KBT forms pure phase perovskite materials through the entire range of *x* with no impurities (Figure S15). Diffraction patterns at room temperature appear cubic when $x < 1$, however Pawley fitting reveals subtle peak splitting of $(111)_c$ and $(002)_c$ reflections when $x \geq 0.7$, indicative of lower symmetry. In (1-*y*)PMN-*y*PT as *y* increases, the structure goes through two monoclinic phases: *Cm* ($y = 0.10 - 0.32$) then to *Pm* ($y = 0.32 - 0.40$).[5,11,12,21] These symmetries are commonly referred to as the M_B (*Cm*) and M_C (*Pm*) phases.[5,11,12,21] Above $y = 0.40$ tetragonal (*P*4*mm*) symmetry is observed. Detailed single phase and multiphase Pawley fitting of SXRD data using the fundamental parameters method with anisotropic strain terms was done to identify symmetries for $x = 0.8$ and 0.9 in (1-*x*)KBMN-*x*KBT (Figure S16-17). Polar subgroups of $Pm\bar{3}m$ which arise from cation displacements were considered.[63] These analyses show that the symmetry lowering observed cannot be explained by *R*3*m* or *P*4*mm* distortions alone; monoclinic symmetries must be employed to describe the profiles observed. The highest quality fits for $x = 0.8$ was found with *Cm* symmetry (Figures 5a, S16) and with *Pm* symmetry for $x = 0.9$ (Figures 5b, S17). Fitting with two low-symmetry phases improved R_{wp}, but increased errors and did not improve the visual fit.

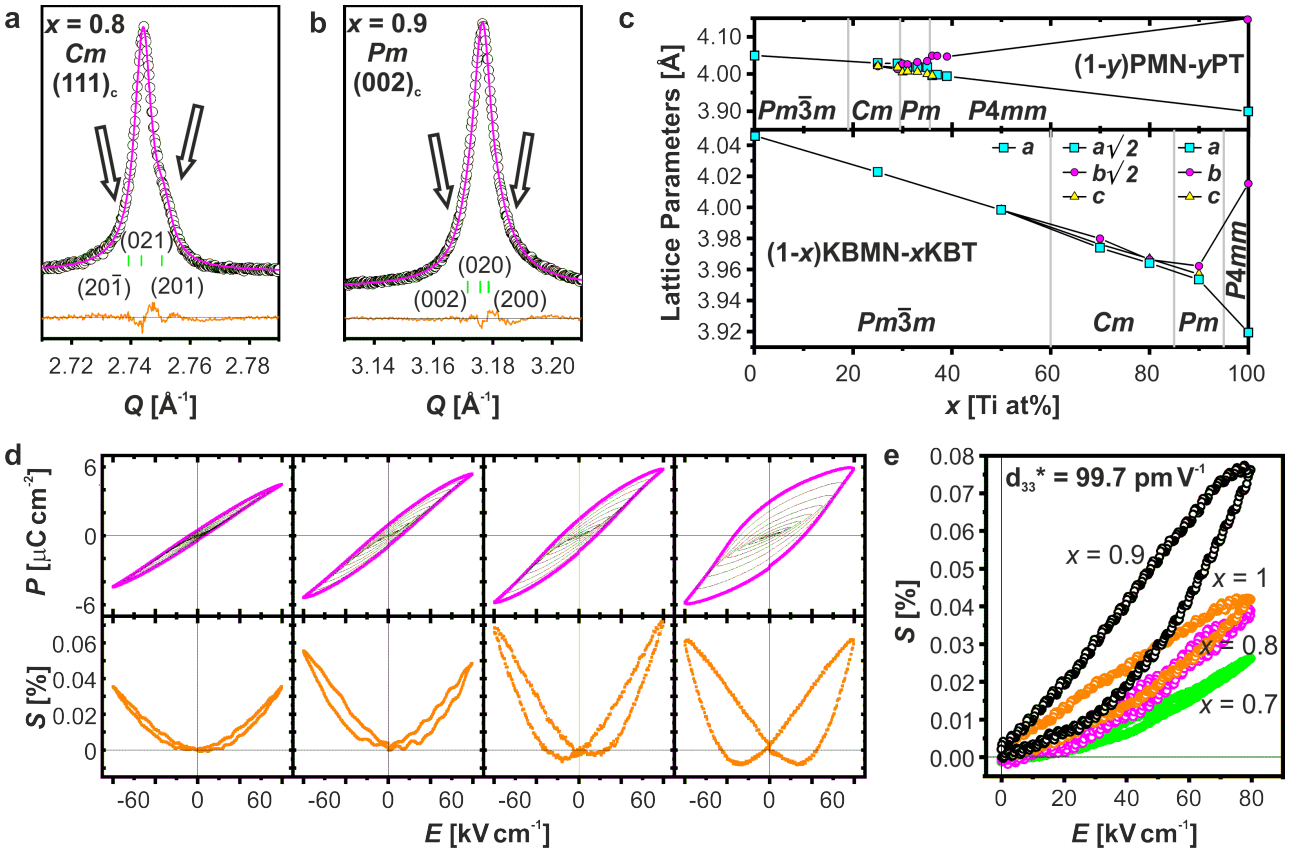

Figure 5. Structure and functional behaviour of the (1-*x*)KBMN-*x*KBT solid solution at room temperature. Pawley fitting of SXRD data showing a) the $(111)_c$ reflection for $x = 0.8$ in Cm symmetry and b) the $(002)_c$ reflection for $x = 0.9$ in Pm symmetry. The observed diffraction data are shown as white circles, the fits are shown as magenta lines, the difference as orange lines, and the *hkl* ticks are shown in green and labelled corresponding to their symmetry. Black arrows have been added to highlight subtle peak broadening that necessitates lower symmetry. c) Lattice parameters for (1-*x*)KBMN-*x*KBT as a function of Ti^{4+} substitution (*x*) with grey lines separating regions with $Pm\bar{3}m$, *Cm*, *Pm*, and *P*4*mm* symmetry. Selected lattice parameters and regions of symmetry, taken from references 11 and 12 for PMN-PT are shown above. All lattice parameters are presented relative to the cubic aristotype and *a*, *b*, and *c* lattice parameters are shown as cyan, yellow, and magenta points respectively. All lattice parameters are summarized in the supporting information. d) The bipolar polarization and strain as a function of electric field, *P*(E) and *S*(E) respectively, for $x = 0.7$, 0.8, 0.9, and 1.0. Lines through $P/S = 0$ and $E = 0$ are shown to illustrate the evolution of linearity in *P*(E) and negative strain in *S*(E). e) Unipolar strain for the same four compositions are shown and the extracted piezoelectric figure of merit for $x = 0.9$ is listed.

to the data. Refined parameters for all samples are tabulated in Tables S11-S18. All data where $x < 0.7$ fit best in $Pm\bar{3}m$ symmetry. Lattice parameters for (1-*x*)KBMN-*x*KBT (Figure 5c) validate the formation of a continuous solid solution and are consistent with previous reports.[26] The evolution of symmetry seen is identical to PMN-PT, but at different quantities of Ti^{4+} substitution. The additional disorder created by $(K_{1/2}Bi_{1/2})^{2+}$ substitution is observed in all aspects of this system: as additional A-site displacements in the refined structure producing extra excess entropy in the heat capacity, a larger ΔT_m, additional Θ_D and Θ_E, and the need for greater quantities of Ti^{4+} substitution to stabilize a ferroelectric ground state.

High temperature ε' and ε'' for samples with $x > 0$ can be seen in Figures S18-23. These data show a T_m which increases with *x*, from 413 K in $x = 0$ to 667 K in KBT. When $x < 1$ T_m is frequency dependent, consistent with relaxor behaviour. ΔT_m decreases with increasing *x*, showing a large decrease from 24 K for $x = 0.8$ to 6 K for $x = 0.9$. In PMN-PT when $y = 0.32 - 1$, T_m is not frequency dependent, and in pure PMN ΔT_m is 18 K, therefore in (1-*x*)KBMN-*x*KBT when $x \leq 0.8$ there is a larger ΔT_m than at any PMN-PT composition.[57,64] Curie-Weiss fitting of dielectric data shows a crossover from negative, antiferroelectric θ_W values to positive, ferroelectric θ_W values for $x \geq 0.5$. The negative θ_W is consistent with the observed diffuse scattering in SAED data for KBMN and furthers the connection with PMN-PT where the suppression of disordered antiferroelectric correlations has been associated with the improved piezoresponse.[21] The divergence of the dielectric data from the Curie-Weiss law (the Burns temperature; T_B) was also extracted. T_B is believed to be the temperature at which dipoles disappear, but the change in T_B with *x* closely follows T_m, indicating that it is likely more associated with the basic chemistry of the system than with dipoles.[35] All parameters extracted from ε' and ε'' are listed in Table S19.

Room temperature polarization ($P(E)$) and strain ($S(E)$) as a function of electric field (Figures 5d, S24-28) measurements confirm that when $x \geq 0.7$ materials have ferroelectric (FE) properties. Hysteresis is observed in $P(E)$ loops and the linearity of loops increase with increasing applied field indicative of FE domain wall motion.[61,65] A current spike appears at about 40 kV cm^{-1} and reveals the coercive field (Figures S24c-28c), a direct observation of FE switching. $P(E)$ loops transition from a slim but not linear shape, characteristic of RFEs, to a classic FE shape with appreciable hysteresis.[15,66] The $S(E)$ also shows a progression from RFE to FE. A "sprout" shaped loop with no negative strain component is seen for $x = 0.7$ and 0.8 characteristic of RFEs. Negative strain is observed at $x = 0.9$ and KBT has a classic FE butterfly shape. The highest strain response in both bipolar and unipolar (Figure 5e) measurements is for $x = 0.9$, which has the same *Pm* symmetry as the MPB composition in PMN-PT ($y = 0.32$). The piezoelectric charge constant (d_{33}) at $x = 0.9$, taken from unipolar strain loops (d_{33}*) shows a modest $d_{33}^* = 99.8$ pm V^{-1}, which is almost double that of $x = 0.8$ or 1. In PMN-PT, the d_{33} of polycrystalline samples are enhanced from $y = 0.28 - 0.45$, and best properties (720 pm V^{-1}) are found in a narrow range within 2% of $y = 0.345$.[7] These measurements show potential for similar property enhancement near the MPB in KBMN-KBT, with composition optimisation over a narrower *x* range and targeted substitution coupled with single crystal growth targets for further research. A greater than expected enhancement of piezoresponse is seen in PMN-PT when moving from ceramics to single crystals. Whether this enhancement is seen in KBMN-KBT should also be explored as it may reveal the mechanistic differences between these materials. There are other figures of merit such as the piezoelectric voltage constant (g_{33}), which is relevant for sensor and energy harvesting applications.[67] The largest piezoelectric voltage constant is also at $x = 0.9$, where $g_{33} = 17.5 \times 10^{-3}$ Vm N^{-1}. This g_{33} makes the performance of KBMN-KBT better than KBT-NBT and $BaTiO_3$ (10.4×10^{-3} and 12.6×10^{-3} Vm N^{-1} respectively), and competitive with optimized PZT and PMN-PT ceramics (19.7×10^{-3} and 21×10^{-3} Vm N^{-1} respectively)[68–70], without further composition optimization of KBMN-KBT.

From these data we construct the KBMN-KBT phase diagram in Figure 6. The phase boundary temperatures have been determined by T_m at 1 MHz, but from our analysis of KBMN it is clear that T_m does not correspond to a structural phase transition but instead to a dipole response. These T_m values are consistent with previous reports.[26] Of note is that the peak in ε' for $x = 0.9$ is at 631 K, which is close to PZT (653 K) and higher than the melting point of electrical solder (450 - 460 K) allowing these materials to be poled prior to device fabrication, a shortcoming of PMN-PT ($y = 0.32$, 430 K) which prevents wide used in devices.[4,5,11,12] Comparing the electromechanical response to the phase diagram, there is a clear peak in response at $x = 0.9$. This region is identified as having *Pm* symmetry. The MPB in PMN-PT is on the *Pm* side of the interface between *Pm* and *Cm* symmetry, and at this point there is a suppression of the relaxor properties.[12] In KBMN-KBT, the degree of dielectric relaxation (ΔT_m) shows a marked decrease at $x = 0.9$, indicating a similar suppression of relaxor behaviour in favour of FE properties. The suppression of relaxor properties is a key distinction of the physics at the MPB in PMN-PT from that of PZT, which is an interface between two FE phases. Finally, the observation of antiferroelectric ordering in dielectric data and its suppression with increased Ti^{4+} substitution is consistent with PMN-PT.[21] Diffuse scattering observed in PMN and PMN-PT single crystals reveals these local antiferroelectric correlations, the suppression of which has been associated with the improved piezoresponse.[21] The impact of these intermediate length-scale interactions needs to be better understood as their signatures are clearly important in both PMN-PT and KBMN-KBT.

With the analogy between KBMN-KBT and PMN-PT established, some differences and opportunities should be discussed. To access the best performance in PMN-PT, single crystals must be used, and these high-performance single crystals are reported to have rhombohedral symmetry.[22] The best performing composition in these single crystals is at y = 0.28. The best performing ceramics have been reported at y = 0.345.[7] The discrepancies in structural assignments and optimal physical response underpins the complexity of these relaxor based systems and the importance of sample state. The underlying physics in PMN-PT as well as PZT is believed to be related to a rotating polarization vector. In both of these models, the properties of experimental samples are optimized when going

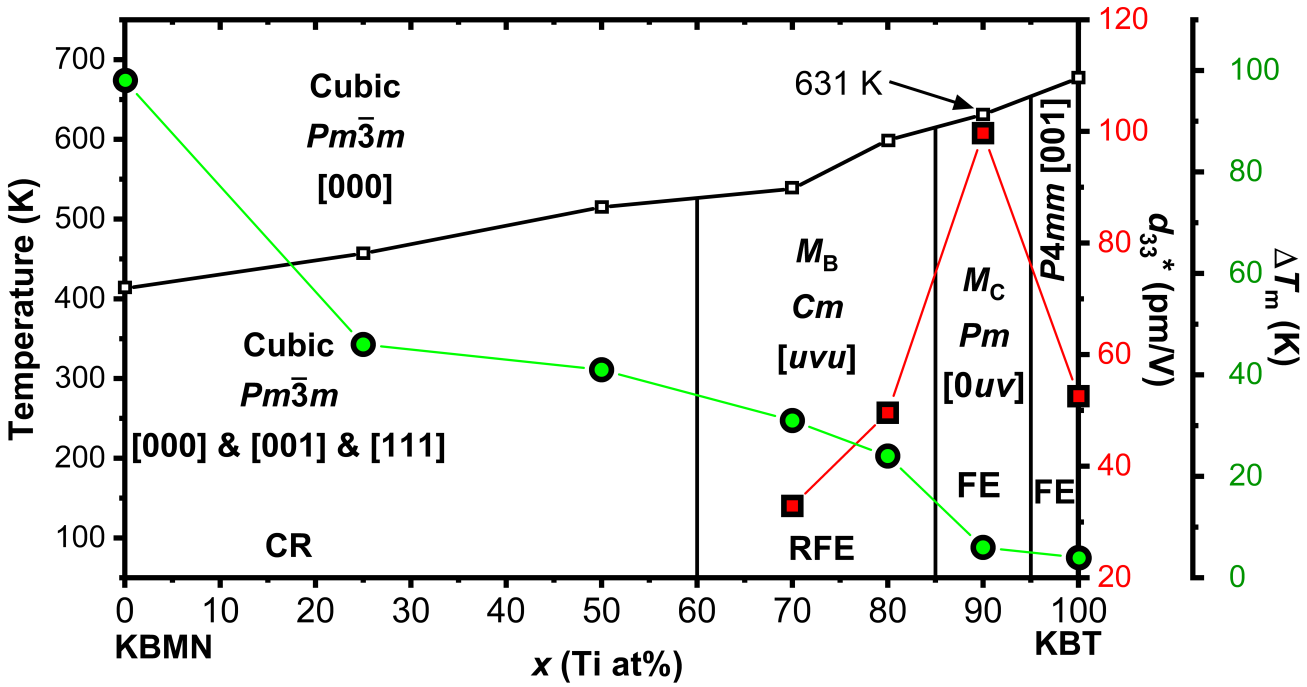

Figure 6. Phase diagram for (1-x)($K_{1/2}Bi_{1/2}$)($Mg_{1/3}Nb_{2/3}$)O_3-x($K_{1/2}Bi_{1/2}$)TiO_3. Phase boundary temperatures are T_m values taken from ε´ measurements at 1 MHz, shown as white squares. The compositional phase boundaries were estimated from both Pawley fitting of XRD data and from the onset of ferroelectric properties. The symmetry of each region is labelled, with monoclinic regions referred to by M_B (*Cm*), and M_C (*Pm*) nomenclature. The polarization directions and regions with CR, RFE, and FE properties are also labelled. The piezoelectric figure of merit (d_{33}*) extracted from unipolar $S(E)$ measurements is shown as red squares. The relaxor character (ΔT_m) taken from dielectric measurements is shown as green circles. The symmetries observed, the suppression of the relaxor character, and the increase in the piezoresponse indicates the same type of MPB seen in PMN-PT.

from a rhombohedral ($R_{[111]}$) to tetragonal ($T_{[001]}$) phase, allowing the full arc of the polarization. The M_a, M_b, and M_c phases represent paths between these $R_{[111]}$ and $T_{[001]}$ phases. Whether the presence of the *M* phases exist homogenously though the sample; are the result of a vector sum between coexisting $R_{[111]}$, $T_{[001]}$ or orthorhombic ($O_{[011]}$) phases[18]; or as interfacial anomalies due to twinned nanodomains[71] is an ongoing debate as to how to appropriately model complexities these materials. Regardless, these *M* phases represent intermediate, and perhaps metastable, phases between $R_{[111]}$ and $T_{[111]}$ phases and therefore facilitate polarization rotation by reducing the activation energy of this change.

CONCLUSIONS

KBMN is a canonical relaxor. The two A-site cations in KBMN that replace the single Pb^{2+} in PMN have distinct structural roles which arise from their different electronic configurations. Spherical s^0 K^+ is located symmetrically at the center of the A-site and inhibits octahedral rotations, while the polarizable s^2 Bi^{3+} undergoes locally polar displacements along two directions to generate lower symmetry environments consistent with the bonding at Bi^{3+} in pure Bi A-site perovskites. The underlying physics is thus not that of PMN, with a single cation producing a single degree of freedom through displacements of a compositionally homogeneous A-site. In KBMN, there are two A-site cations, one of which is active and executes two distinct displacements that relax involving two degrees of freedom, while the second cation remains locally undistorted, increases heterogeneity in the system, and prevents octahedral rotations. The greater diversity of local environments in KBMN is identified by diffraction, dielectric, and heat capacity analysis and can now be used to control the functional response with substitution approaches that will need to differ from those in Pb-based systems because of the distinct chemistry if they are to fully exploit that difference. The identification of a Pb-free CR with its analogies to and the differences from PMN presents opportunities for material discovery, optimization, and understanding of the complex physics driving relaxor phenomena. The identification of one A-site, with two cations, and three environments also presents opportunities for inorganic solid state materials design beyond dielectric and piezoelectric materials. KBMN enables the formation of a Pb-free analogue of the PMN-PT piezoelectric family through solid solution with a ferroelectric with the same polarization direction as $PbTiO_3$. Although the phenomenology is identical (symmetries at and suppression of relaxation mechanisms near the MPB, presence of antiferroelectric correlations) the quantitative behaviour is not as the extent of relaxation and number of degrees of freedom are greater in KBMN. This difference in physics can be traced to the distinct chemistry produced by the substitution that affords KBMN, driven by heterogeneity of dipolar displacements on the A-site, which are a component of the chemical heterogeneity that yields three locally different A-site environments because of the simultaneous presence of s^2 and s^0 cations. The CR-FE canonical relaxor-ferroelectric MPB strategy for Pb-free piezoelectrics is complementary to the well-studied FE-FE (or AFE-FE) PZT-based approach and may benefit from the diversity of A-site displacements

that could be used to generate relaxors tuned to match an accessible FE polarisation direction. The control of local A-site chemistry by electronic configuration in perovskites offers a distinct route to Pb-free piezoelectrics through relaxor formation.

ASSOCIATED CONTENT

Supporting Information

The Supporting Information is available free of charge on the ACS Publications website.

Spark plasma sintering details, compositional analysis details, crystallographic details, low temperature XRD data and dielectric, ferroelectric and piezoelectric data (PDF)

AUTHOR INFORMATION

Corresponding Author

* m.j.rosseinsky@liverpool.ac.uk

Notes

The authors declare no competing financial interests.

Underlying data is available at http://datacat.liverpool.ac.uk/id/eprint/1041

ACKNOWLEDGMENT

We thank EPSRC (EP/R011753 and EP/R010293) for funding this research. J.G. and Q.G. thank EP/N004884. We thank STFC for access to Polaris (Xpress proposal 1890309) and Dr. Ron Smith for collecting the data and performing absorption corrections. We thank Argonne National Lab for access to the 11BM beamline (Rapid Access proposal 65125) and to Dr. Saul Lapidus and Dr. Lynn Ribaud for collecting the data.

REFERENCES

(1) Manjón-Sanz, A. M.; Dolgos, M. R. Applications of Piezoelectrics: Old and New. *Chem. Mater.* **2018**, *30* (24), 8718–8726.

(2) Noheda, B. Structure and High-Piezoelectricity in Lead Oxide Solid Solutions. *Curr. Opin. Solid State Mater. Sci.* **2002**, *6* (1), 27–34.

(3) Damjanovic, D.; Klein, N.; Li, J.; Porokhonskyy, V. What Can Be Expected from Lead-Free Piezoelectric Materials? *Funct. Mater. Lett.* **2010**, *3* (1), 5–13.

(4) Jaffe, B.; Cook, W. R.; Jaffe, H. L. *Piezoelectric Ceramics*; Academic Press: New York, 1971.

(5) Noheda, B.; Cox, D. E.; Shirane, G.; Gao, J.; Ye, Z. G. Phase Diagram of the Ferroelectric Relaxor (1-x)$PbMg_{1/3}Nb_{2/3}O_3$-X$PbTiO_3$. *Phys. Rev. B* **2002**, *66*, 1–10.

(6) Noheda, B.; Cox, D. E. Bridging Phases at the Morphotropic Boundaries of Lead Oxide Solid Solutions. *Phase Transitions* **2006**, *79* (1–2), 5–20.

(7) Kelly, J.; Leonard, M.; Tantigate, C.; Safari, A. Effect of Composition on the Electromechanical Properties of (1-x)Pb($Mg_{1/3}Nb_{2/3}$)O_3-X$PbTiO_3$ Ceramics. *J. Am. Ceram. Soc.* **1997**, *80* (4), 957–964.

(8) Bell, A. J. On the Origin of the Large Piezoelectric Effect in Morphotropic Phase Boundary Perovskite Single Crystals. *Appl. Phys. Lett.* **2000**, *76* (1), 109–111.

(9) Damjanovic, D. Contributions to the Piezoelectric Effect in Ferroelectric Single Crystals and Ceramics. *J. Am. Ceram. Soc.* **2005**, *88* (10), 2663–2676.

(10) Zhang, N.; Yokota, H.; Glazer, A. M.; Ren, Z.; Keen, D. A.; Keeble, D. S.; Thomas, P. A.; Ye, Z. G. The Missing Boundary in the Phase Diagram of $PbZr_{1-x}Ti_xO_3$. *Nat. Commun.* **2014**, *5*, 1–9.

(11) Singh, A. K.; Pandey, D.; Zaharko, O. Powder Neutron Diffraction Study of Phase Transitions in and a Phase Diagram of (1-x)[$PbMg_{1/3}Nb_{2/3}O_3$]-X$PbTiO_3$. *Phys. Rev. B* **2006**, *74*, 1–18.

(12) Phelan, D.; Rodriguez, E. E.; Gao, J.; Bing, Y.; Ye, Z. G.; Huang, Q.; Wen, J.; Xu, G.; Stock, C.; Matsuura, M.; Gehring, P. M. Phase Diagram of the Relaxor Ferroelectric (1-x)Pb($Mg_{1/3}Nb_{2/3}$)O_3-X$PbTiO_3$ Revisited: A Neutron Powder Diffraction Study of the Relaxor Skin Effect. *Phase Transitions* **2015**, *88* (3), 283–305.

(13) Bokov, A. A.; Ye, Z. Dielectric Relaxation in Relaxor Ferroelectrics. *J. Adv. Dielectr.* **2012**, *02* (02), 1241010.

(14) Bokov, A. A.; Ye, Z. G. Recent Progress in Relaxor Ferroelectrics with Perovskite Structure. *J. Mater. Sci.* **2006**, *41* (1), 31–52.

(15) Li, F.; Zhang, S.; Damjanovic, D.; Chen, L. Q.; Shrout, T. R. Local Structural Heterogeneity and Electromechanical Responses of Ferroelectrics: Learning from Relaxor Ferroelectrics. *Adv. Funct. Mater.* **2018**, *28* (37), 1–21.

(16) Eremenko, M.; Krayzman, V.; Bosak, A.; Playford, H. Y.; Chapman, K. W.; Woicik, J. C.; Ravel, B.; Levin, I. Local Atomic Order and Hierarchical Polar Nanoregions in a Classical Relaxor Ferroelectric. *Nat. Commun.* **2019**, *10* (1), 1–9.

(17) Li, F.; Cabral, M. J.; Xu, B.; Cheng, Z.; Dickey, E. C.; LeBeau, J. M.; Wang, J.; Luo, J.; Taylor, S.; Hackenberger, W.; Bellaiche, L.; Xu, Z.; Chen, L.-Q.; Shrout, T. R.; Zhang, S. Giant Piezoelectricity of Sm-Doped $PbMg_{1/3}Nb_{2/3}O_3$-$PbTiO_3$ Single Crystals. *Science (80-.).* **2019**, *364*, 264–258.

(18) Li, F.; Lin, D.; Chen, Z.; Cheng, Z.; Wang, J.; Li, C.; Xu, Z.; Huang, Q.; Liao, X.; Chen, L. Q.; Shrout, T. R.; Zhang, S. Ultrahigh Piezoelectricity in Ferroelectric Ceramics by Design. *Nat. Mater.* **2018**, *17* (4), 349–354.

(19) Li, F.; Zhang, S.; Yang, T.; Xu, Z.; Zhang, N.; Liu, G.; Wang, J.; Wang, J.; Cheng, Z.; Ye, Z. G.; Luo, J.; Shrout, T. R.; Chen, L. Q. The Origin of Ultrahigh Piezoelectricity in Relaxor-Ferroelectric Solid Solution Crystals. *Nat. Commun.* **2016**, *7*, 1–9.

(20) Hou, D.; Usher, T. M.; Fulanovic, L.; Vrabelj, M.; Otonicar, M.; Ursic, H.; Malic, B.; Levin, I.; Jones, J. L. Field-Induced Polarization Rotation and Phase Transitions in 0.70Pb($Mg_{1/3}Nb_{2/3}$) O_3-0.30$PbTiO_3$ Piezoceramics Observed by in Situ High-Energy x-Ray Scattering. *Phys. Rev. B* **2018**, *97* (21), 1–9.

(21) Krogstad, M. J.; Gehring, P. M.; Rosenkranz, S.; Osborn, R.; Ye, F.; Liu, Y.; Ruff, J. P. C.; Chen, W.; Wozniak, J. M.; Luo, H.; Chmaissem, O.; Ye, Z. G.; Phelan, D. The Relation of Local Order to Materials Properties in Relaxor Ferroelectrics. *Nat. Mater.* **2018**, *17* (August), 718–724.

(22) Qiu, C.; Wang, B.; Zhang, N.; Zhang, S.; Liu, J.; Walker, D.; Wang, Y.; Tian, H.; Shrout, T. R.; Xu, Z.; Chen, L. Q.; Li, F. Transparent Ferroelectric Crystals with Ultrahigh Piezoelectricity. *Nature* **2020**, *577* (7790), 350–354.

(23) Takenaka, H.; Grinberg, I.; Liu, S.; Rappe, A. M. Slush-like Polar Structures in Single-Crystal Relaxors. *Nature* **2017**, *546* (7658), 391–395.

(24) Takenaka, T.; Maruyama, K.; Sakata, K. ($Bi_{1/2}Na_{1/2}$)TiO_3-$BaTiO_3$ System for Lead-Free Piezoelectric Ceramics. *Jpn. J. Appl. Phys.* **1991**, *30* (9B), 2236–2239.

(25) Isupov, V. A. Ferroelectric $Na_{0.5}Bi_{0.5}TiO_3$ and $K_{0.5}Bi_{0.5}TiO_3$ Perovskites and Their Solid Solutions. *Ferroelectrics* **2005**, *315* (773559934), 123–147.

(26) Yamada, Y.; Akutsu, T.; Asada, H.; Nozawa, K.; Hachiga, S.; Kurosaki, T.; Ikagawa, O.; Hiroyuki, F.; Hozumi, K.; Kawamura, T.; Amakawa, T.; Hirota, K.; Ikeda, T. Effect of B-Ions Substitution in [($K_{1/2}Bi_{1/2}$)-($Na_{1/2}Bi_{1/2}$)](Ti-B)O_3 System with B = Zr, $Fe_{1/2}Nb_{1/2}$, $Zn_{1/3}Nb_{2/3}$, or $Mg_{1/3}Nb_{2/3}$. *Jpn. J. Appl. Phys.* **1995**, *34* (9), 5462–6466.

(27) Ishii, Y.; Nomura, K.; Fukuda, F.; Asada, H.; Aihara, T.; Mochizuki, S.; Hiroyuki, F.; Amakawa, T.; Kitami, M.; Hirota, K.; Ikeda, T. B-Ion Substitution in (Pb-A)(Ti-B)O_3 Systems with A = $Na_{1/2}Bi_{1/2}$ or $K_{1/2}Bi_{1/2}$ and B = Zr, $Fe_{1/2}Nb_{1/2}$, $Zn_{1/3}Nb_{2/3}$, or $Mg_{1/2}W_{1/2}$. *Jpn. J. Appl. Phys.* **1995**, *34* (9), 4849–4853.

(28) Swartz, S. L.; Shrout, T. R. Fabrication of Perovskite Lead Magnesium Niobate. *Mater. Res. Bull.* **1982**, *17* (10), 1245–1250.

(29) Coelho, A. Whole-Profile Structure Solution from Powder Diffraction Data Using Simulated Annealing. *J. Appl. Crystallogr.* **2000**, *33* (3 Part 2), 899–908.

(30) Stephens, P. W. Phenomenological Model of Anisotropic Peak Broadening in Powder Diffraction. *J. Appl. Crystallogr.* **1999**, *32* (2), 281–289.

(31) Petrícek, V.; Dušek, M.; Palatinus, L. Crystallographic Computing System JANA2006: General Features. *Zeitschrift fur Krist.* **2014**, *229* (5), 345–352.

(32) Van Smaalen, S.; Palatinus, L.; Schneider, M. The Maximum-Entropy Method in Superspace. *Acta Crystallogr. Sect. A Found. Crystallogr.* **2003**, *59* (5), 459–469.

(33) Momma, K.; Izumi, F. VESTA 3 for Three-Dimensional Visualization of Crystal, Volumetric and Morphology Data. *J. Appl. Crystallogr.* **2011**, *44* (6), 1272–1276.

(34) Elliott, C.; Vijayakumar, V.; Zink, W.; Hansen, R. National Instruments LabVIEW: A Programming Environment for Laboratory Automation and Measurement. *J. Assoc. Lab. Autom.* **2007**, *12* (1), 17–24.

(35) Toulouse, J. The Three Characteristic Temperatures of Relaxor Dynamics and Their Meaning. *Ferroelectrics* **2008**, *369* (1), 203–213.

(36) Phillips, W. A. Tunneling States in Amorphous Solids. *J. Low Temp. Phys.* **1972**, *7* (3–4), 351–360.

(37) Tachibana, M.; Takayama-Muromachi, E. Thermal Conductivity and Heat Capacity of the Relaxor Ferroelectric $[PbMg_{1/3}Nb_{2/3}O_3]_{1-x}[PbTiO_3]_x$. *Phys. Rev. B* **2009**, *79* (10), 1–4.

(38) Bonneau, P.; Garnier, P.; Calvarin, G.; Husson, E.; Gavarri, J. R.; Hewat, A. W.; Morell, A. X-Ray and Neutron Diffraction Studies of the Diffuse Phase Transition in Ceramics. *J. Solid State Chem.* **1991**, *91* (2), 350–361.

(39) Bonneau, P.; Garnier, P.; Husson, E.; Morell, A. Structural Study of PMN Ceramics by X-Ray Diffraction between 297 and 1023 K. *Mater. Res. Bull.* **1989**, *24* (2), 201–206.

(40) Perrin, C.; Menguy, N.; Suard, E.; Muller, C.; Caranoni, C.; Stepanov, A. Neutron Diffraction Study of the Relaxor – Ferroelectric Phase Transition in Disordered $Pb(Sc_{1/2}Nb_{1/2})O_3$. *J. Phys. Condens. Matter* **2000**, *12*, 7523–7539.

(41) Surta, T. W.; Manjón-Sanz, A.; Qian, E.; Tran, T. T.; Dolgos, M. R. Low Temperature Synthesis Route and Structural Characterization of $(Bi_{0.5}A_{0.5})(Sc_{0.5}Nb_{0.5})O_3$ (A = K^+ and Na^+) Perovskites. *Inorg. Chem. Front.* **2018**, *5*, 1033–1044.

(42) Dolgos, M.; Adem, U.; Wan, X.; Xu, Z.; Bell, A. J.; Comyn, T. P.; Stevenson, T.; Bennett, J.; Claridge, J. B.; Rosseinsky, M. J. Chemical Control of Octahedral Tilting and Off-Axis A Cation Displacement Allows Ferroelectric Switching in a Bismuth-Based Perovskite. *Chem. Sci.* **2012**, *3* (5), 1426–1435.

(43) Itoh, K.; Zeng, L. Z.; Nakamura, E.; Mishima, N. Crystal Structure of $BaTiO_3$ in the Cubic Phase. *Ferroelectrics* **1985**, *63*, 29–37.

(44) Malibert, C.; Dkhil, B.; Kiat, J. M.; Durand, D.; Berar, J. F.; Spasojevic de Bire, A. Order and Disorder in the Relaxor Ferroelectric Perovskite $PbSc_{1/2}Nb_{1/2}O_3$ (PSN): Comparison with Simple Perovskites $BaTiO_3$ and $PbTiO_3$. *J. Phys. Condens. Matter* **1997**, *9*, 7485–7500.

(45) Suchomel, M. R.; Fogg, A. M.; Allix, M.; Niu, H.; Claridge, J. B.; Rosseinsky, M. J. Bi_2ZnTiO_6: A Lead-Free Closed-Shell Perovskite with a Calculated Ionic Polarization of 150 $MCcm^{-2}$. *Chem. Mater.* **2006**, *18*, 4987–4989.

(46) Haumont, R.; Kornev, I. A.; Lisenkov, S.; Bellaiche, L.; Kreisel, J.; Dkhil, B. Phase Stability and Structural Temperature Dependence in Powdered Multiferroic BiFeO3. *Phys. Rev. B* **2008**, *78* (13), 1–8.

(47) Bhakar, A.; Pandey, A. H.; Singh, M. N.; Upadhyay, A.; Sinha, A. K.; Gupta, S. M.; Ganguli, T. Structural Analysis of Lead Magnesium Niobate Using Synchrotron Powder X-Ray Diffraction and the Rietveld Method. *Acta Crystallogr. Sect. B Struct. Sci. Cryst. Eng. Mater.* **2016**, *72*, 404–409.

(48) Shoto, K.; Eisuke, M.; Chikako, M.; Yoshihiro, K.; Nao, T.; Hiroshi, T.; Sachiko, M.; Masaki, T.; Satoshi, W. Electronic Polarization in $KNbO_3$ Visualized by Synchrotron Radiation Powder Diffraction. *Jpn. J. Appl. Phys.* **2013**, *52* (9S1), 09KF04.

(49) Krayzman, V.; Levin, I.; Woicik, J. C.; Bridges, F. Correlated Rattling-Ion Origins of Dielectric Properties in Reentrant Dipole Glasses $BaTiO_3$-$BiScO_3$. *Appl. Phys. Lett.* **2015**, *107* (19), 7–12.

(50) Levin, I.; Krayzman, V.; Woicik, J. C.; Bridges, F.; Sterbinsky, G. E.; Usher, T. M.; Jones, J. L.; Torrejon, D. Local Structure in $BaTiO_3$-$BiScO_3$ Dipole Glasses. *Phys. Rev. B* **2016**, *93* (10), 1–12.

(51) Levin, I.; Keeble, D. S.; Cibin, G.; Playford, H. Y.; Eremenko, M.; Krayzman, V.; Laws, W. J.; Reaney, I. M. Nanoscale Polar Heterogeneities and Branching Bi-Displacement Directions in $K_{0.5}Bi_{0.5}TiO_3$. *Chem. Mater.* **2019**, *31* (7), 2450–2458.

(52) Miao, S.; Zhu, J.; Zhang, X.; Cheng, Z. Y. Electron Diffraction and HREM Study of a Short-Range Ordered Structure in the Relaxor Ferroelectric $Pb(Mg_{1/3}Nb_{2/3})O_3$. *Phys. Rev. B* **2002**, *65* (5), 1–4.

(53) Husson, E.; Chubb, M.; Morell, A. Superstructure in $PbMg_{1/3}Nb_{2/3}O_3$ Ceramics Revealed by High Resolution Electron Microscopy. *Mater. Res. Bull.* **1988**, *23* (3), 357–361.

(54) Chen, J.; Chan, H. M.; Harmer, M. P. Ordering Structure and Dielectric Properties of Undoped and La/Na-Doped $Pb(Mg_{1/3}Nb_{2/3})O_3$. *J. Am. Ceram. Soc.* **1989**, *72* (4), 593–598.

(55) Kopecký, M.; Kub, J.; Fábry, J.; Hlinka, J. Nanometer-Range Atomic Order Directly Recovered from Resonant Diffuse Scattering. *Phys. Rev. B* **2016**, *93* (5), 1–8.

(56) Paciak, M.; Welberry, T. R.; Kulda, J.; Kempa, M.; Hlinka, J. Polar Nanoregions and Diffuse Scattering in the Relaxor Ferroelectric $PbMg_{1/3}Nb_{2/3}O_3$. *Phys. Rev. B* **2012**, *85* (22), 1–9.

(57) Tsurumi, T.; Soejima, K.; Kamiya, T.; Daimon, M. Mechanism of Diffuse Phase Transition in Relaxor Ferroelectrics. *Jpn. J. Appl. Phys.* **1994**, *33*, 1959–1964.

(58) Butcher, S. J.; Thomas, N. W. Ferroelectricity in the System $Pb_{1-x}Ba_x(Mg_{1/3}Nb_{2/3})O_3$. *J. Phys. Chem. Solids* **1991**, *52* (4), 595–601.

(59) Cohen, R. E. Origin of Ferroelectricity in Perovskite Oxides. *Nature* **1992**, *358* (6382), 136–138.

(60) Viehland, D.; Wuttig, M.; Cross, L. E. The Glassy Behavior of Relaxor Ferroelectrics. *Ferroelectrics* **1991**, *120* (1), 71–77.

(61) Li, S.; Cao, W.; Cross, L. E. The Extrinsic Nature of Nonlinear Behavior Observed in Lead Zirconate Titanate Ferroelectric Ceramic. *J. Appl. Phys.* **1991**, *69* (10), 7219–7224.

(62) Gorev, M. V.; Flerov, I. N.; Bondarev, V. S.; Sciau, P. Heat Capacity Study of Relaxor $PbMg_{1/3}Nb_{2/3}O_3$ in a Wide Temperature Range. *J. Exp. Theor. Phys.* **2003**, *96* (3), 531–537.

(63) Howard, C. J.; Stokes, H. T. Structures and Phase Transitions in Perovskites - A Group-Theoretical Approach. *Acta Crystallogr. Sect. A* **2005**, *61* (1), 93–111.

(64) Grinberg, I.; Juhás, P.; Davies, P. K.; Rappe, A. M. Relationship between Local Structure and Relaxor Behavior in Perovskite Oxides. *Phys. Rev. Lett.* **2007**, *99* (26), 1–4.

(65) Dolgos, M. R.; Adem, U.; Manjón-Sanz, A.; Wan, X.; Comyn, T. P.; Stevenson, T.; Bennett, J.; Bell, A. J.; Tran, T. T.; Halasyamani, P. S.; Claridge, J. B.; Rosseinsky, M. J. Perovskite B-Site Compositional Control of $[110]_p$ Polar Displacement Coupling in an Ambient-Pressure-Stable Bismuth-Based Ferroelectric. *Angew. Chemie - Int. Ed.* **2012**, *51* (43), 10770–10775.

(66) Jin, L.; Li, F.; Zhang, S. Decoding the Fingerprint of Ferroelectric Loops: Comprehension of the Material Properties and Structures. *J. Am. Ceram. Soc.* **2014**, *97* (1), 1–27.

(67) Xu, T. B. *Energy Harvesting Using Piezoelectric Materials in Aerospace Structures*; 2016.

(68) Uchino, K. *Ferroelectric Devices*; 2009.

(69) Kunnath, N.; Philip, J. Nanostructured Ceramics of Potassium Sodium Bismuth Titanate: Hydrothermal Synthesis and Piezoelectric Response at Morphotropic Phase Boundary. *New J. Glas. Ceram.* **2019**, *09* (01), 1–14.

(70) Yan, Y.; Wang, Y. U.; Priya, S. Electromechanical Behavior of [001]-Textured $Pb(Mg_{1/3}Nb_{2/3})O_3$-$PbTiO_3$ Ceramics. *Appl. Phys. Lett.* **2012**, *192905* (100), 1–4.

(71) Wang, Y. U. Diffraction Theory of Nanotwin Superlattices with Low Symmetry Phase: Application to Rhombohedral Nanotwins and Monoclinic M_A and M_B Phases. *Phys. Rev. B* **2007**, *76* (2), 1–11.

For Table of Contents Only